JOURNAL OF SPACECRAFT AND ROCKETS
Vol. 47, No. 3, May–June 2010

Unsteady Supersonic Flows over a Backward-Facing Step with Applied Magnetic Field

Ovais U. Khan* and Klaus A. Hoffmann†
Wichita State University, Wichita, Kansas 67260-0044

DOI: 10.2514/1.42190

Time-dependent behavior of shock/boundary-layer interaction has been investigated numerically for flows over a backward-facing step. Using a multiblock-grid strategy, the global domain of computation has been decomposed into two subdomains representing upstream and downstream regions from the step location. First, Navier–Stokes analysis has been performed to investigate the unsteady shock/boundary-layer interaction. Subsequently, magneto-fluid-dynamics computations have been performed to explore the effects of applied magnetic field over the unsteady nature of the problem and its use for local flow control. A time-explicit modified Runge–Kutta scheme with total-variation-diminishing limiters under a multiblock-grid approach has been implemented. The governing equations are composed of the Navier–Stokes equation modified to include the effect of magnetic field under low-magnetic-Reynolds-number approximation. The effects of an applied magnetic field and a time-dependent magnetic field on the flowfield have been investigated. It has been shown that the application of magnetic field increases the unsteady nature of the problem.

Nomenclature

$\bar{\mathbf{A}}, \bar{\mathbf{B}}$ = Jacobian matrices
$\mathbf{B}$ = $\{B_x, B_y, B_z\}$, magnetic field vector, T
$\mathbf{E}$ = $\{E_x, E_y, E_z\}$, electric field vector, V/m
$\mathbf{E}$ = $\{E\}_{5\times1}$, flux vector component in the x direction
$\mathbf{E}_v$ = $\{E_v\}_{5\times1}$, diffusion flux vector in the x direction
e_t = total energy, J
$\mathbf{F}$ = $\{F\}_{5\times1}$, flux vector component in the y direction
$\mathbf{F}_v$ = $\{F_v\}_{5\times1}$, diffusion flux vector in the y direction
$\bar{\mathbf{I}}$ = identity tensor
J = Jacobian of transformation
$\mathbf{J}$ = current density vector, A/m^2
M = Mach number
p = pressure, Pa
$\mathbf{Q}$ = $\{Q\}_{5\times1}$, field vector
Re_∞ = freestream Reynolds number
R_m = magnetic Reynolds number
t = time, s
$\mathbf{U}$ = $\{u, v, w\}$, velocity vector, m/s
x, y = Cartesian coordinates
γ = ratio of specific heats
η = generalized coordinate
μ_{e0} = free-space magnetic permeability, H/m
ξ = generalized coordinate
ρ = density, Kg/m^3
σ_e = electrical conductivity, S/m
$\boldsymbol{\nabla}$ = nabla vector

Subscripts

e = electromagnetic quantity
v = diffusion quantity
∞ = freestream condition

I. Introduction

WITHIN the last few decades, several experimental and theoretical investigations have been undertaken to determine the flow characteristics and associated heat transfer rates for supersonic flows over a backward-facing step. It has been widely accepted that fluid dynamics problems associated with supersonic separated flows are highly time-dependent and may involve complex shock/boundary-layer interaction.

Numerous studies have highlighted this important aspect. Hartfield et al. [1] developed a planer measurement technique with laser-induced iodine fluorescence for the measurement of supersonic flow over a backward-facing step. Their results provided an insight to flow characteristics and properties for a supersonic combustor that agreed with analytical and numerical simulations. The data were obtained for approximately 1 min exposure on the collection array camera and time-averaged accordingly. A time-averaged measurement technique over collected images was employed with the assumption of long exposure time versus characteristic flow times. They discussed factors that contributed to uncertainties affecting the measured data and identified time-averaged measurement technique as one of them.

Using time-accurate scheme and employing adaptive unstructured grids Loth et al. [2] performed large eddy simulation of supersonic flows over axisymmetric backward-facing step for a range of Mach numbers. They reported that formation of large eddies and the unsteady nature of the problem cause intense mixing-layer fluctuations; thus, time-averaging of the fully developed computations is necessary to compare the results with time-averaged experimental data. The developed algorithm was based on a shock-capturing scheme that adds nonlinear contribution through flux-corrected transport scheme. Euler equations for compressible flow are discretized using a finite element technique.

In an attempt to validate several computational fluid dynamics codes for modeling hypersonic flows, Ebrahimi [3–5] performed a series of tasks. Several cases of engineering applications including supersonic flows over rearward-facing steps were considered to determine the validity of different computer codes for predicting the expansion-fan region, compression effects of shock, and relatively uniform pressure between the shock and shear layer. Results were compared with the experimental data. Two supersonic Mach numbers of 2.5 and 3.5 were considered for all the investigations with different turbulence models. The results indicated some over-prediction in surface pressure at the separation region; however, analyses were in good agreement in the flow-reattachment region.

Presented as Paper 0396 at the 45th AIAA Aerospace Sciences Meeting and Exhibit, Reno, NV, 8–11 January 2007; received 14 November 2008; revision received 26 October 2009; accepted for publication 10 November 2009.

*Postdoctoral Research Fellow, Department of Aerospace Engineering. Student Member AIAA.

†Marvin J. Gordon Distinguished Professor, Department of Aerospace Engineering. Associate Fellow AIAA.

In an attempt to introduce different error indicators for adaptive remeshing algorithms for hybrid grids, Yang [6–8] performed a series of numerical investigations. A remeshing strategy of unstructured grid for modeling supersonic backward-facing-step flows was introduced [6]. An extended locally implicit scheme with dissipation model was developed to solve unsteady Euler equations. Different grids strategies were used to achieve a match with the experimental pressure distributions beyond the rearward-facing step. Subsequent to performing initial simulation on a nonadaptive mesh, an adaptive mesh strategy based on the error indicator was used for further simulations. For an adaptive grid, the number of triangles and quadrilaterals were controlled by a modified error indicator that contained unified magnitudes of density gradient and gradient of vorticity. Several hybrid meshes were investigated to capture the physics of the problem and to obtain a better resolution of the flowfield. It was reported that a dense mesh at the corner and at the regions where strong convective fluxes occurred is necessary to capture the circulation zone and to enhance the accuracy of the results. An adaptive mixed triangular-quadrilateral grid with increased number of cells at the zones of intense flow variations (corner vortex, expansion fan, and oblique shock wave) was recommended to perform the analysis within a reasonable amount of time.

Subsequently, viscous terms were added to the Euler model and turbulence effects were introduced in the adaptive remeshing algorithm [7]. The modified error indicator incorporates unified magnitude of substantial derivatives of pressure and vorticity for controlling the grid spacing. Unsteady mass-averaged Navier–Stokes equations with a low-Reynolds-number k-ε turbulence model were used with a locally implicit scheme. Similar conclusions to that of the previous work of [6] have been reported.

In [8], two error indicators for achieving adaptive grids in the regions of severe flow variations were developed. Supersonic turbulent flow over a rearward-facing step with time-dependent mass-averaged Navier–Stokes equations was considered. Initially, analyses were performed on an unstructured mesh composed of relatively coarse quadrilateral and triangular elements. Regardless of the poor resolution of the flowfield, a reasonable solution was obtained. Finally, adaptive refined unstructured meshes were generated for subsequent numerical experiments, resulting in high-resolution solution. Despite differences observed in the downstream pressure near the upper-wall region of flow, their calculated pressure distributions for refined mesh agreed well with the experimental data.

Recently, Hermann et al. [9] presented a flow simulation methodology (FSM) for investigating the time-dependent behavior of complex compressible turbulent flows for subsonic and supersonic flow regimes. Subsonic flow over backward-facing step and two-dimensional bluff bodies were considered, and axisymmetric wake flow (axisymmetric backward-facing-step flow) was modeled under the supersonic flow regime. A contribution function was developed to allow a consistent transition between Reynolds-averaged Navier–Stokes and direct numerical simulations within the same computation, depending on the local flow behavior and physical resolution. Time-dependent simulations were carried out and time-averaged results were presented with turbulence effects. Good agreement of FSM with direct numerical simulation was achieved for supersonic axisymmetric backward-facing-step flow.

The effects of applied magnetic fields over supersonic-backward-facing-step flows were recently investigated by Khan and Hoffmann [10]. Different orientations of magnetic field distributions were discussed. A multiblock solver based on modified Runge–Kutta scheme with total-variation-diminishing (TVD) limiters was developed and successfully implemented under a low-magnetic-Reynolds-number assumption. The Navier–Stokes computation was in good agreement with the analytical and experimental data available in the literature. For magneto-fluid-dynamics (MFD) analysis, three types of magnetic field distributions were implemented. Increase in the size of circulation region, movement of shock toward the exit section, increase in shock wave angle, and decrease in flow velocity were observed after the application of magnetic field. For the uniform magnetic field distribution, an increase in pressure levels occurred over the entire domain, whereas for dipole magnetic field distributions, only increases in pressures at the circulation region or in the neighborhood of the dipole location were achieved. Higher strengths of uniform magnetic fields and higher strengths of dipole magnetic fields in the vicinity of the step caused an increase in the shock thickness. It was found that enlargement in the size of separation bubble is highly dependent on the type and strength of magnetic field intensity.

The impact of applied electromagnetic fields over high-speed flowfields that involve shock/boundary-layer interaction has been investigated by several authors: MacCormack [11–13], Shang et al. [14,15], Gaitonde and Poggie [16], Poggie and Gaitonde [17,18], Damevin and Hoffman [19], and Khan et al. [20,21]. It has been reported that the application of magnetic field results in delaying the boundary-layer separation, decrease in surface heat transfer, increase in the thrust, and flow-compression phenomenon.

A review of the available literature related to the backward-facing-step flows reveals that the investigation to incorporate local flow control by applied magnetic field is lacking. The flowfield associated with the high-speed supersonic flow over a backward-facing step is one of the most complex problems that occur in several applications. Incorporation of local flow control becomes critical in many applications with similar geometries. Thus, the objective of the current efforts is to explore local flow control by application of magnetic field. Most of the problems involving shock/boundary-layer interaction are naturally unsteady; therefore, in this investigation the effects of applied magnetic field have been investigated with an emphasis on exploring the unsteady nature of the problem. MFD analysis has been preformed with uniform and time-dependent magnetic field distributions with a low-magnetic-Reynolds-number assumption. The governing equations and the numerical schemes are reviewed in the following sections.

II. Governing Equations

The viscous MFD equations under low-magnetic-Reynolds-number assumption are as follows.

Continuity equation:

$$\frac{\partial \rho}{\partial t} + \nabla \cdot (\rho \mathbf{U}) = 0 \tag{1}$$

Momentum equation:

$$\frac{\partial (\rho \mathbf{U})}{\partial t} + \nabla \cdot [\rho \mathbf{U} \otimes \mathbf{U} + p \bar{\bar{\mathbf{I}}}] = \mathbf{J} \times \mathbf{B} + \nabla \cdot \bar{\bar{\boldsymbol{\tau}}} \tag{2}$$

where Ohm's law indicates that

$$\mathbf{J} = \sigma_e [\mathbf{E} + \mathbf{U} \times \mathbf{B}] \tag{3}$$

Energy equation:

$$\frac{\partial}{\partial t}(\rho e_t) + \nabla \cdot [(\rho e_t + p)\mathbf{U}] = \mathbf{E} \cdot \mathbf{J} + \nabla \cdot (\bar{\bar{\boldsymbol{\tau}}} \cdot \mathbf{U}) + \nabla \cdot \mathbf{q} \tag{4}$$

where

$$\rho e_t = \frac{1}{2}\rho(u^2 + v^2 + w^2) + \frac{p}{\gamma - 1} \tag{5}$$

The equations are presented in nondimensional form; details are provided in [19]. The governing equations are rearranged in a compact flux vector formulation as follows:

$$\frac{\partial \mathbf{Q}}{\partial t} + \frac{\partial \mathbf{E}}{\partial x} + \frac{\partial \mathbf{F}}{\partial y} = \frac{\partial \mathbf{E}_v}{\partial x} + \frac{\partial \mathbf{F}_v}{\partial y} + \mathbf{S}_{\mathrm{MFD}} \tag{6}$$

where $\mathbf{Q}$ is the unknown vector,

$$\mathbf{Q} = [\rho \quad \rho u \quad \rho v \quad \rho w \quad \rho e_t]^T \tag{7a}$$

$\mathbf{E}$, $\mathbf{F}$, and $\mathbf{E}_v$, $\mathbf{F}_v$, are the inviscid and viscous flux vectors, respectively; the details of each flux vector can be found in [10]. The additional source term is represented by $\boldsymbol{S}_{\mathrm{MFD}}$:

$$S_{\mathrm{MFD}} = R_m \begin{bmatrix} 0 \\ (\mathbf{J}\times\mathbf{B})_x \\ (\mathbf{J}\times\mathbf{B})_y \\ (\mathbf{J}\times\mathbf{B})_z \\ (\mathbf{J}\times\mathbf{B})\cdot\mathbf{U} + \frac{1}{\sigma_e}\mathbf{J}\cdot\mathbf{J} \end{bmatrix} \tag{7b}$$

Subscripts x, y, and z indicate the vector components in the respective directions. The governing Eq. (6) is transformed from the physical space to a computational space and expressed as

$$\frac{\partial\bar{\mathbf{Q}}}{\partial t} + \frac{\partial\bar{\mathbf{E}}}{\partial\xi} + \frac{\partial\bar{\mathbf{F}}}{\partial\eta} = \frac{\partial\bar{\mathbf{E}}_v}{\partial\xi} + \frac{\partial\bar{\mathbf{F}}_v}{\partial\eta} + \bar{\mathbf{S}}_{\mathrm{MFD}} \tag{8}$$

where

$$\bar{\mathbf{Q}} = \frac{\mathbf{Q}}{J} \tag{9a}$$

$$\bar{\mathbf{S}}_{\mathrm{MFD}} = \frac{1}{J}\mathbf{S}_{\mathrm{MFD}} \tag{9b}$$

$\bar{\mathbf{E}}$, $\bar{\mathbf{F}}$, and $\bar{\mathbf{E}}_v$, $\bar{\mathbf{F}}_v$, represent the transformed convective and diffusive flux terms, respectively. Each flux vector has five components, and $\bar{\mathbf{S}}_{\mathrm{MFD}}$ represents the transformed electromagnetic source term. The MFD equation (8) can be rewritten as follows by definition of the Jacobian matrices:

$$\frac{\partial\bar{\mathbf{Q}}}{\partial t} + \bar{\mathbf{A}}\frac{\partial\bar{\mathbf{Q}}}{\partial\xi} + \bar{\mathbf{B}}\frac{\partial\bar{\mathbf{Q}}}{\partial\eta} = \frac{\partial\bar{\mathbf{E}}_v}{\partial\xi} + \frac{\partial\bar{\mathbf{F}}_v}{\partial\eta} + \bar{\mathbf{S}}_{\mathrm{MFD}} \tag{10}$$

where details of transformation metrics $\bar{\mathbf{A}}$ and $\bar{\mathbf{B}}$ are provided in [20].

III. Computational Methodology

The modified Runge–Kutta scheme augmented with TVD limiters is used to obtain numerical solutions under multiblock strategy. The global domain has been decomposed into two subdomains representing upstream and downstream regions with respect to the step location. Data are transferred through connecting interface of the domains. The numerical scheme for the low-magnetic-Reynolds-number approach is expressed as

$$\bar{\mathbf{Q}}^{(0)}_{i,j} = \bar{\mathbf{Q}}^{n}_{i,j} \tag{11a}$$

for $m = 1$ to 4

$$\bar{\mathbf{Q}}^{(m)}_{i,j} = \bar{\mathbf{Q}}^{n}_{i,j} - \frac{\Delta t}{\alpha_m}\left(\frac{\partial\bar{\mathbf{E}}}{\partial\xi} + \frac{\partial\bar{\mathbf{F}}}{\partial\eta} - \frac{\partial\bar{\mathbf{E}}_v}{\partial\xi} - \frac{\partial\bar{\mathbf{F}}_v}{\partial\eta} - \bar{\mathbf{S}}_{\mathrm{MHD}}\right)^{(m-1)}_{i,j} \tag{11b}$$

$$\bar{\mathbf{Q}}^{n+1}_{i,j} = \bar{\mathbf{Q}}^{(4)}_{i,j} + \overline{\mathbf{TVD}}^{n} \tag{11c}$$

where superscript n represents time level and $\alpha_m = 4$ to 1. The TVD model is based on the eigenstructure of the convective flux Jacobian matrices. For the low-magnetic-Reynolds-number approximation, the eigenstructure and numerical method are the same as those used for Euler equations. In the current investigation, the Davis–Yee symmetric TVD scheme is implemented; further details can be found in [20].

IV. Results and Discussions

Numerical simulations of supersonic flow over a backward-facing step are provided in this section. Geometry and freestream operating conditions have been set according to the experimental work of Hartfield et al. [1]. Laminar flow conditions of calorically perfect gas are assumed. Details of geometry and operating conditions are provided in Table 1.

The computational grid is shown in Fig. 1; the domain upstream of the step is extended up to a sufficient length to include any upstream effects. Similarly, downstream of the step is extended to model the expected variations that may occur by the application of magnetic field. Grid clustering is enforced at the base and near the wall regions to accurately capture the large gradients. It should be noted that present computations have been performed for a flow exposed to an unconfined environment; in contrast, the experiment in [1] was performed for confined environment.

Table 1 Geometry and freestream conditions

Geometry details	Operating conditions
Step height: 3.18 mm	Mach number: $M_\infty = 2.0$
Upstream length: 20.12 mm	Pressure: $p_\infty = 34.8$ kPa
Downstream length: 40.12 mm	Temperature: $T_\infty = 294.0$ K
Downstream height: 18.56 mm	Reynolds number: $Re_\infty = 1.033 \times 10^5$

A. Boundary Conditions

In computational fluid dynamics applications, boundary conditions become extremely important to guarantee a stable and converged solution. It is a requirement that must be satisfied by dependent variables and their derivatives at the domain's boundary. In the current investigation, the specified supersonic freestream conditions are imposed at the inlet. No-slip velocity, zero pressure gradient, and adiabatic-wall boundary conditions have been applied at the solid wall. All primitive variables have been extrapolated from the flowfield over the exit and upper-boundary sections.

It is important to mention that a concrete validation of the developed code was performed in [10] with the experimental data for the Navier–Stokes analysis. However, due to the requirement of large number of grid points associated with shock/boundary-layer interaction, a grid independence test has been performed to obtain an efficient and economical grid.

B. Grid Independence Test

A grid independence test is necessary to identify a mesh that can provide economical and reliable data for further numerical investigation. Pressure at the horizontal surface downstream of the base has been chosen for the grid independence investigation, since the region near the base downstream of the step is exposed to the most critical flow conditions. Figure 2 represents the pressure distribution obtained from the Navier–Stokes solution along the horizontal surface downstream of the step for different grid spacing. Pressure remains approximately uniform in the recirculation region and subsequently increases to a higher value, consistent with the inviscid oblique shock solution. It is worthwhile to note that the difference in pressure values is large at the beginning of the recompression region for different grid spacing. Thus, more grid points have been introduced at this region to attain better accuracy. Finally, a convergence in pressure values is achieved with the increase in grid points. Since pressure distribution obtained with the grid size of 160 × 96 coincides with the grid size of 150 × 90, a grid spacing of 150 × 90 has been chosen for all subsequent analyses. The corresponding grid spacing for the upstream domain is set to 75 × 46.

C. Navier–Stokes Analysis

As a first step, the Navier–Stokes equations are solved within the specified domain with local time-stepping, and the converged solution is presented in Fig. 3. The complex nature of the flowfield is evident in the vicinity of the backward-facing step. Formation of the expansion fan at the corner is obvious with the leading expansion

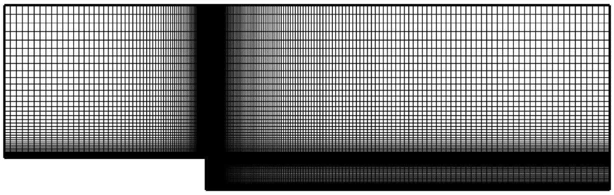

Fig. 1 Multiblock clustered grid for the computational analysis.

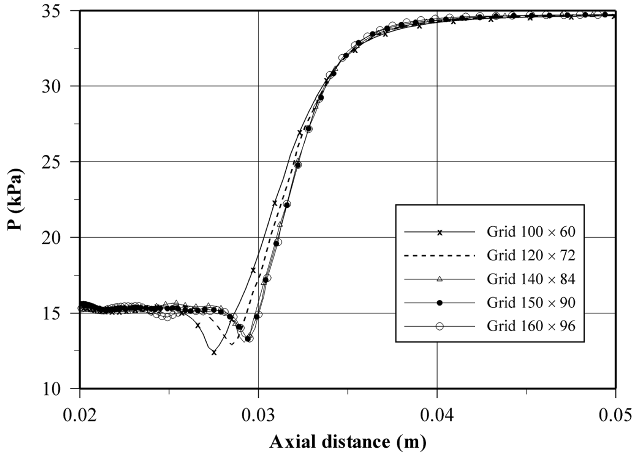

Fig. 2 Comparison of pressure distributions obtained with different grid spacing.

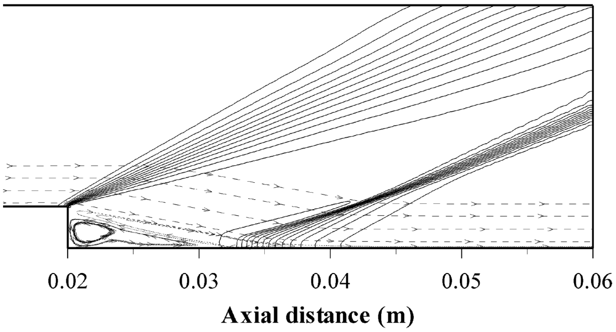

Fig. 3 Pressure contours obtained from the Navier–Stokes computation.

wave at approximately 30°, which is in agreement with the analytical value of 30° obtained for an inviscid supersonic flow. A circulation region at the base corner that contains fairly uniform pressure distribution is also evident in the figure; a free shear layer separates the circulation region from the flow downstream of the base surface. Furthermore, the appearance of an oblique shock wave through coalescence of compression waves in the further downstream region is apparent. Flow deflection through the expansion fan and subsequent attainment of a freestream direction through the oblique shock wave is also visible in the figure.

D. Unsteady Analysis

The time-dependent behavior of shock/boundary-layer interaction is presented in this section. The converged result is used as the initial condition to proceed further toward unsteady solution, with a constant time step over the entire domain. The pressure contours along with the velocity streamlines for the Navier–Stokes analysis at different time levels are shown in Fig. 4. Flow separation and reattachment can be easily observed in the figure. A combination of two vortices is evident for all time intervals; the lower vortex is referred to as the primary vortex and the upper vortex is referred to as the secondary vortex.

A detailed examination of unsteady simulations indicates some extension and contraction in the size of circulation bubble. For example, Figs. 4b and 4c depict small displacements of shock wave toward the exit section for time intervals of 1.0 and 5.0 ms, respectively, which are occurring primarily due to increase in the size of circulation bubble. Further time increment ($t = 8.0$ ms) has resulted in the contraction of circulation bubble; thus, movement of shock wave toward the corner takes place, as shown in Fig. 4d.

Shock displacement becomes more visible in Fig. 5, which illustrates nondimensional pressure distribution along the horizontal surface downstream of the step for different time periods. Differences in the base pressure are also evident with respect to different time intervals; nevertheless, the same levels of pressures are obtained beyond the shock wave. It is important to note that variations in base pressure depend on the size of circulation bubble. That is, the size of circulation zone is larger at 5.0 ms than at 0.0 ms. Change in the circulation region affects the turning of streamlines and the expansion fan, thus affecting the base pressure. Thus, a relatively larger circulation bubble obtained at 5.0 ms implies that less flow expansion has occurred at the base region compared to that at 0.0 ms. Finally, for the 8.0 ms case, contraction of the zone has caused more flow expansion compared to the 5.0 ms case, thus producing a drop in base pressure that ultimately results in movement of the shock toward the initial position.

E. Magneto-Fluid-Dynamic Analysis

In this section, the unsteady behavior of the supersonic flow over the backward-facing step has been explored under applied magnetic fields. Electrical conductivity of gas in the upstream domain is set to zero, and a low value of electrical conductivity is assumed in the downstream domain, resulting in a magnetic Reynolds number equal to 0.01 based on the step height. This low value of magnetic Reynolds number ensures a negligibly induced magnetic field compared to the applied magnetic field; hence, low-magnetic-Reynolds-number formulation is selected because of

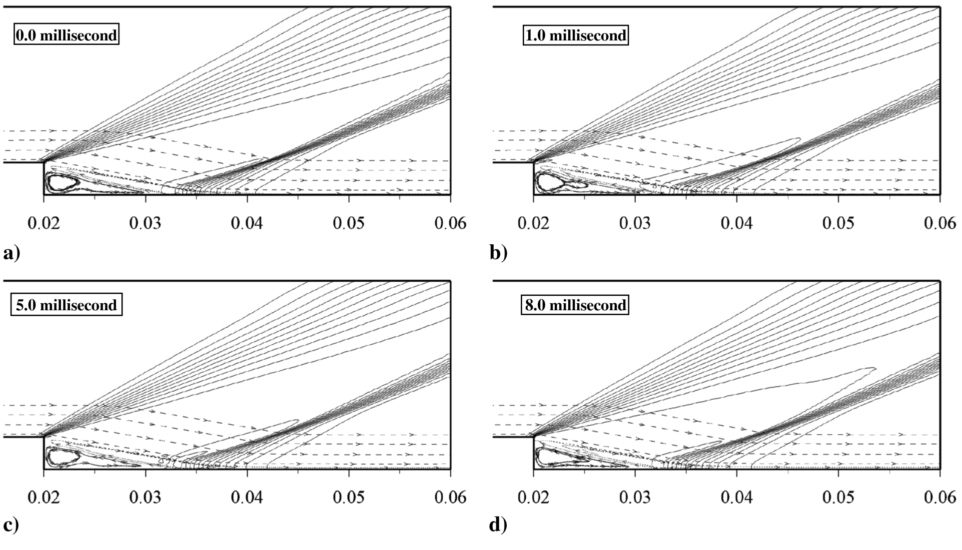

Fig. 4 Comparison of the Navier–Stokes pressure contours at different intervals of time.

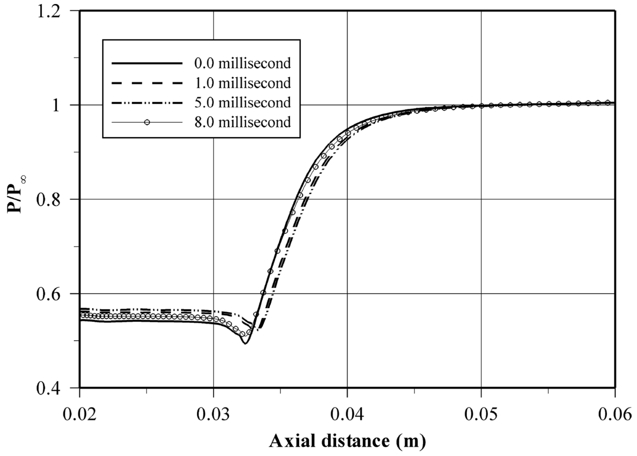

Fig. 5 Pressure distribution along horizontal surface for different intervals of time obtained from the Navier–Stokes analysis.

its simplicity and efficiency. Both time-independent and time-dependent uniform magnetic field distributions along the *y* direction are imposed. The applied electric field is set equal to zero in the present investigation.

The first set of magneto-fluid-dynamics (MFD) computation consists of the application of magnetic field perpendicular to the freestream flow, as shown in Fig. 6. The magnetic field is attenuated far downstream before the exit to prevent flow separation at the exit location. The applied magnetic field has a uniform value from $x = 20$ to 30 mm and decreases linearly to zero from $x = 30$ to 50 mm.

Figure 7 shows pressure contours obtained with uniform magnetic field strengths of 0.4 T imposed along the *y* direction; local time-stepping is used to achieve the converged solution. A combination of primary and secondary vortices has occurred, similar to the previous Navier–Stokes computations. Comparison with the converged Navier–Stokes solution indicates a change in the flow structure after the application of the magnetic field, due to the presence of the Lorentz force. It has been found that the expansion fan and oblique shock wave become steeper and thicker with respect to the Navier–Stokes prediction following the application of a magnetic field. In addition, the Lorentz force has produced resistive effects on the flow velocity field that ultimately result in an increase in pressure level downstream of the step over the entire domain.

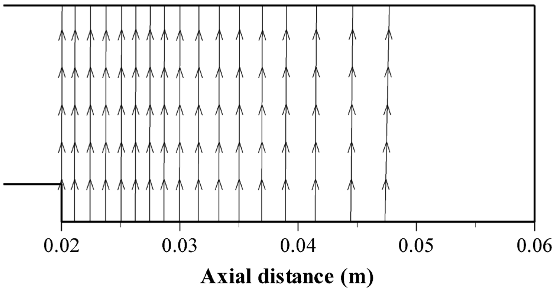

Fig. 6 Uniform applied magnetic field distribution along the *y* direction.

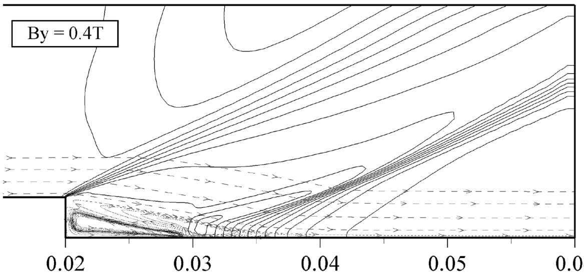

Fig. 7 Pressure contours obtained from MFD analysis.

1. *Unsteady MFD Analysis*

Subsequently, computations have been initiated to investigate the unsteady behavior of this complex flow problem with applied magnetic field. The converged MFD flow result obtained with $By =$ 0.4 T has been used to initiate the time-accurate solution. Solutions have been obtained at various time intervals. Figure 8 shows pressure contours along with streamlines for MFD analysis at different time intervals; $t = 0.0$ ms represents the converged solution. Results are presented for relatively longer periods of time, because substantial variations occur for time-accurate MFD calculations compared with the Navier–Stokes calculations. Interestingly, an increase in the unsteady nature of the problem is observed with the application of the magnetic field; that will enhance mixing and may provide benefits in some applications. From Fig. 8b at $t = 1.0$ ms, it is obvious that the size of the circulation bubble has increased and the primary vortex translates from the corner to the root of the shock wave, resulting in substantial shock displacement toward the exit section. Further time increment at $t = 5.0$ ms (Fig. 8c) has resulted in additional movement of the primary vortex, thereby causing further enlargement in the circulation bubble, and more displacement of shock to the exit region has eventually occurred. No major development in the flow structure is observed for $t = 8.0$ ms computation, as shown in Fig. 8d. That is, at 8.0 ms, the size of the circulation zone and shock location remain similar to that at 5.0 ms. However, at 9.0 ms, contraction in the circulation zone begins to occur, as depicted in Fig. 8e. It can be observed that primary vortex translates back to the corner, causing reduction in the size of the circulation bubble, thus resulting in shock movement toward the corner. Likewise, additional time development has resulted in further contraction of the bubble, as shown in Fig. 8f for the 16 ms case, resulting in an approximately similar shock/expansion-fan structure and circulation-zone size compared to Fig. 8a.

Figure 9 depicts the time development of horizontal surface pressure at the downstream of the step for MFD calculations. It has been observed that the largest circulation zone occurs for the 5.0 ms case, which results in the lowest drop in pressure after crossing the expansion fan and maximum movement of the shock toward the exit section. Subsequently, shock remains at the same vicinity up to 8.0 ms and thereafter moves toward the step with a drop in base pressure, attaining the same value as that of 0.0 ms. It is interesting to observe that for all time intervals, pressure variations are occurring after the expansion fan; however, recovery in pressures to a similar value is achieved downstream beyond the shock wave. Noteworthy is the fact that unsteady behavior is primarily due to enlargement and contraction of the circulation bubble. A large bubble causes less flow expansion, and thus higher pressure in the base region and shock wave movement toward the exit section takes place. Similar behavior was observed in the Navier–Stokes analysis, except bubble oscillations with respect to time were small compared to MFD analysis.

2. *Time-Dependent Magnetic Field Distribution*

The second set of MFD analysis employs time-varying magnetic field distribution. Spatial magnetic field variations are set according to the distribution illustrated in Fig. 6; however, magnetic field strength varies with respect to time according to the function shown in Fig. 10 for a period of 0.0 to 0.1 ms.

Figure 11 shows pressure contours along with streamlines for time-dependent magnetic field variations. At 0.0 ms, the applied magnetic field is zero and no change in flowfield is observed compared to the converged Navier–Stokes solution, as shown in Fig. 11a; however, with the increment of time, the effects of magnetic field accumulation become evident. For example, at 0.04 ms, the variation in the flowfield is higher than the variation occurred at 0.02 ms.

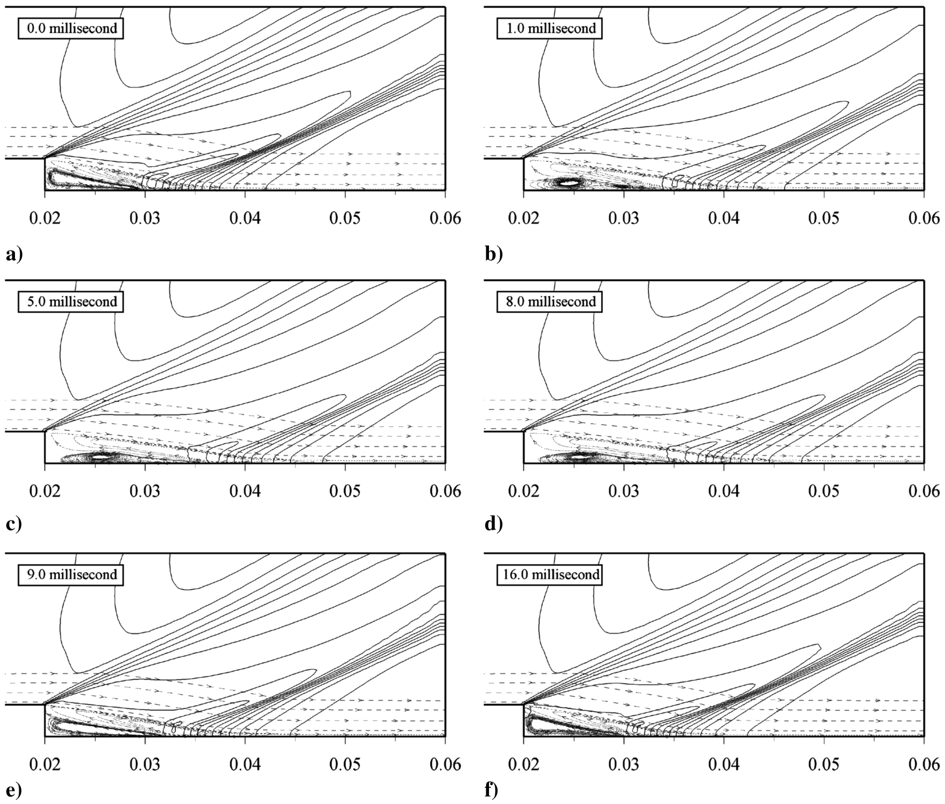

Fig. 8 Comparison of pressure contours obtained from MFD analysis at different intervals of time.

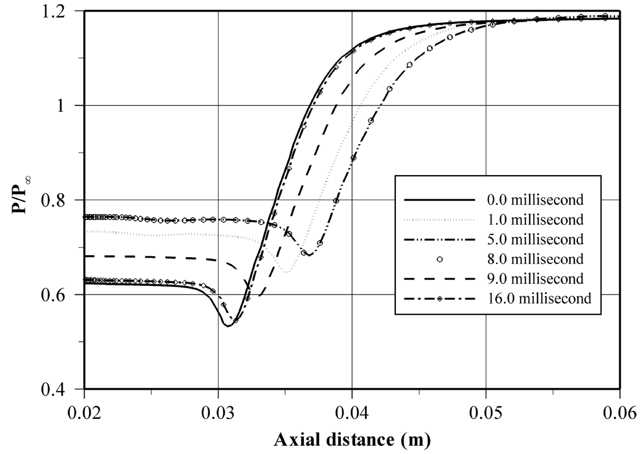

Fig. 9 Pressure distribution along horizontal surface for different time intervals obtained from MFD analysis.

The changes that occurred after the application of magnetic field include distortions in the Prandtl–Mayer expansion fan and shock wave structure and increase in the size of separation bubble, depending upon the magnetic field intensity. Figure 11b indicates the initial stage of these variations, and subsequent buildup is obvious from Figs. 11c–11f. A close examination of Figs. 11c and 11d indicates an increase in the angle of the leading Mach wave and weakening of the oblique shock wave. Further time increment results in coalescence of compression waves into a normal shock at the upper boundary and total dissipation of oblique shock wave, as depicted from Figs. 11e and 11f for 0.08 and 0.1 ms, respectively. Likewise, the recirculation region has been substantially disturbed with the increase of time interval for the present transient magnetic field distribution, which is obvious through all images of Fig. 11. At 0.02 ms, a relatively smaller recirculation zone exists; however, at 0.1 ms it attains its largest size.

It is interesting to note that the applied magnetic field at 0.1 ms time interval is zero; however, variations in flow structure still exist, which is primarily due to the buildup of applied magnetic effects in a short period of time. These effects were dissipated and recovery of the original shock/expansion-fan structure was achieved after some period of time when the strength of magnetic field became zero at 0.1 ms. To illustrate this point, time-accurate computation has been performed by using the flow data available at 0.1 ms as the initial condition. Figure 12 shows the pressure distribution obtained after a 2.5 ms period of time without magnetic field effects. It is worthwhile to note that full recovery of the flow structure has been achieved and the accumulated magnetic field effects have been dissipated. The recovered flowfield has an expansion fan at the corner, circulation zone, and reattached shock wave, similar to the Navier–Stokes solution.

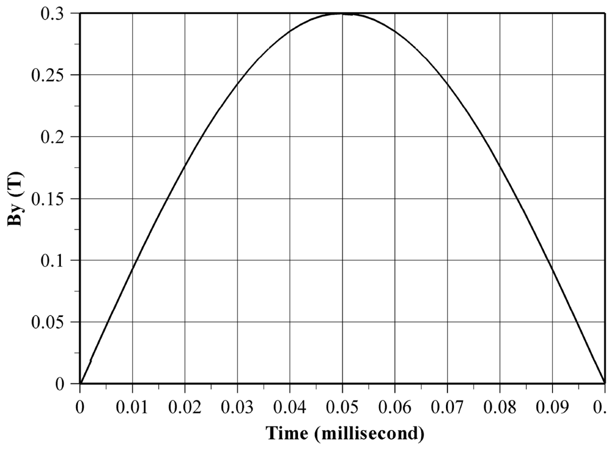

Fig. 10 Time-dependent magnetic field distribution.

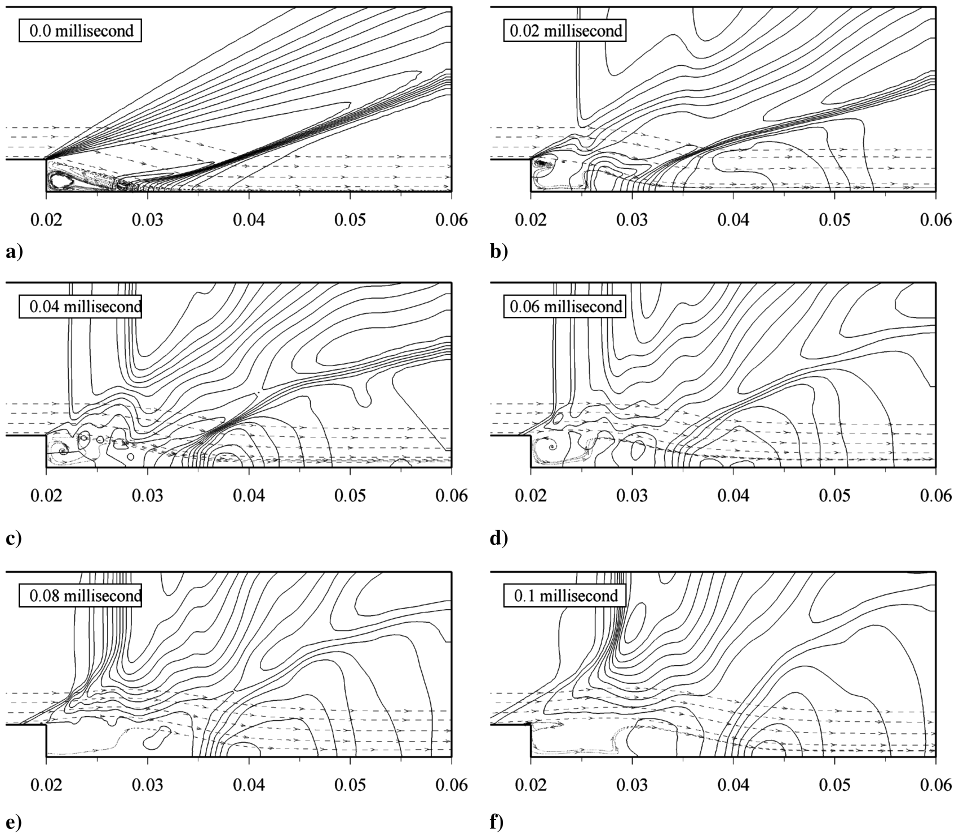

Fig. 11 Pressure contours obtained at different time intervals for time-dependent magnetic field application.

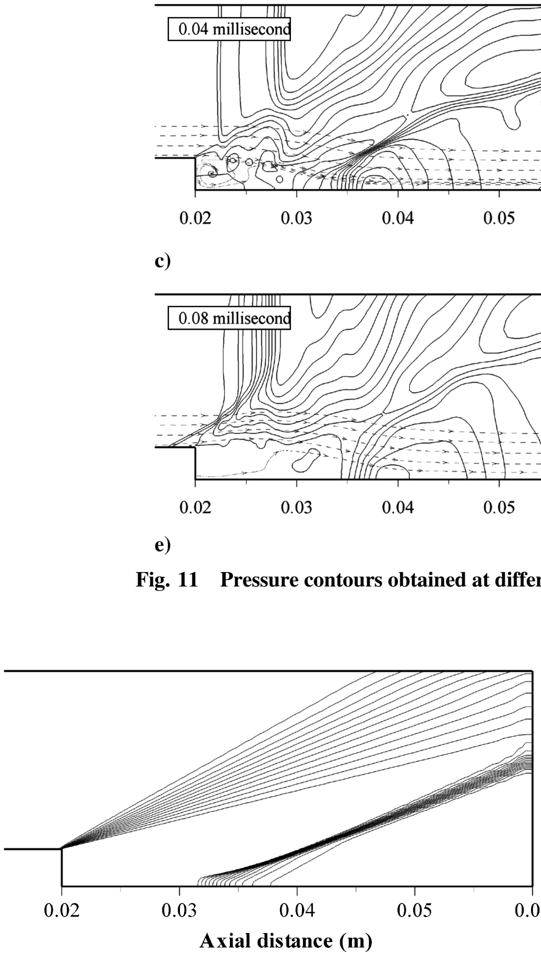

Fig. 12 Pressure contours obtained after 2.5 ms time interval without magnetic field application.

V. Conclusions

Unsteady behavior of high-speed supersonic flows over a rearward-facing step with and without applied magnetic field has been explored. The low-magnetic-Reynolds-number approach has been used to simulate the effects of applied magnetic fields. Using multiblock technique, a four-stage modified Runge–Kutta scheme with TVD limiters is used to numerically solve the governing MFD equations. Both uniform and transient magnetic field distributions have been implemented. Small oscillations in oblique shock wave location are observed due to small expansion and contraction in the size of circulation bubble for the unsteady Navier–Stokes analysis. Application of a uniform magnetic field has caused a change in the flow structure in the entire domain, displacement of oblique shock wave, increase in oblique shock wave angle, and decrease in flow velocity in the plasma domain. Noteworthy is the fact that changes in circulation bubble were small for the unsteady Navier–Stokes analysis; however, unsteady MFD computations have shown substantial increase in the amplitude of shock oscillations, due to large expansion and contraction of separation bubble observed after the application of magnetic field. Moreover, the application of time-dependent magnetic field distribution for a short period of time has caused substantial disturbances in the flowfield downstream of the step. Dissipation of expansion fan and oblique shock wave has taken place due to accumulation of magnetic field effects; however, full recovery of flow structure is achieved when computation has been performed for a long period of time without magnetic field application. Based on the results for time-accurate MFD calculations, it can be deduced that application of magnetic field has increased the unsteadiness of present flow regime. Moreover, the increase in unsteady nature of the problem may provide some potential to enhance the mixing phenomenon for a typical shock/boundary-layer interaction problem.

Acknowledgment

The authors acknowledge the support of the Wichita State University High Performance Computing Center for conducting the computational tasks.

References

[1] Hartfield, R. J., Hollo, S. D., and McDaniel, J. C., “Planar Measurement Technique for Compressible Flow Using Laser Induced Fluorescence,” *AIAA Journal*, Vol. 31, No. 3, 1993, pp. 483–490. doi:10.2514/3.11355

[2] Loth, E., Kailasanath, K., and Löhner, R., “Supersonic Flow over an Axisymmetric Backward-Facing Step,” *Journal of Spacecraft and Rockets*, Vol. 29, No. 3, May–June 1992, pp. 352–359. doi:10.2514/3.26358

[3] Ebrahimi, H. B., “CFD Validation for Scramjet Combustor and Nozzle Flows, Part I,” AIAA Paper 1993-1840, 1993.

[4] Ebrahimi, H. B., “CFD Validation and Evaluation for Combustor and Nozzle Flow, Part II,” AIAA Paper 1994-0025, 1994.

[5] Ebrahimi, H. B., “CFD Validation and Evaluation for Reacting Flows, Part III,” AIAA Paper 1995-0735, 1995.

[6] Yang, S. Y., “Remeshing Strategy of the Supersonic Flow over a Backward-Facing Step,” *The Chinese Journal of Mechanics (Series A)*, Vol. 18, No. 3, Sept. 2002, pp. 127–138.

[7] Yang, S. Y., “Remeshing Strategy of the Supersonic Turbulent Flow over a Backward-Facing Step,” *Numerical Heat Transfer*, Part B,

Vol. 46, 2004, pp. 79–99.
doi:10.1080/10407790490430615

[8] Yang, S. Y., "Adaptive Strategy of the Supersonic Turbulent Flow over a Backward-Facing Step," *International Journal for Numerical Methods in Fluids*, Vol. 44, 2004, pp. 1163–1184.
doi:10.1002/fld.694

[9] Hermann, F. F., Dominic, A. V., and Richard, D. S., "A Methodology for Simulating Compressible Turbulent Flows," *Journal of Applied Mechanics*, Vol. 73, May 2006, pp. 405–412.
doi:10.1115/1.2150231

[10] Khan, O. U., and Hoffmann, K. A., "Flow Control over a Backward-Facing Step with Application of a Magnetic Field," *Journal of Spacecraft and Rockets*, Vol. 45, No. 2, March–April, 2008, pp. 255–263.
doi:10.2514/1.30097

[11] MacCormack, R. W., "Aerodynamic Flow Calculations with Strong Magnetic Induction and Diffusion," AIAA Paper 2005-0559, 2005.

[12] MacCormack, R. W., "Simulation of Hypersonic Flow About an Air Vehicle with Strong Magnetic Field Interaction," AIAA Paper 2006-3232, 2006.

[13] MacCormack, R. W., "Numerical Simulation of Aerodynamic Flow Within a Strong Magnetic Field with Hall Current and Ion Slip," AIAA Paper 2007-4370, 2007.

[14] Shang, J. S., Canupp, P. W., and Gaitonde, D. V., "Computational Magneto-Aerodynamic Hypersonics," AIAA Paper 1999-4903, 1999.

[15] Shang, J. S., Hayes, J., Menart, J., and Miller, J., "Blunt Body in Hypersonic Electromagnetic Flow Field," *Journal of Aircraft*, Vol. 40, No. 2, March–April 2003, pp. 314–322.
doi:10.2514/2.3095

[16] Gaitonde, D. V., and Poggie, J., "Simulations of Magnetogasdynamic Flow Control Techniques," AIAA Paper 2000-2326, 2000.

[17] Poggie, J., and Gaitonde, D. V., "Magnetic Control of Hypersonic Blunt Body Flow," AIAA Paper 2000-0452, 2000.

[18] Poggie, J., and Gaitonde, D. V., "Magnetic Control of Flow Past a Blunt Body: Numerical Validation and Exploration," *Physics of Fluids*, Vol. 14, No. 5, May 2002, pp. 1720–1731.
doi:10.1063/1.1465424

[19] Damevin, H. M., and Hoffmann, K. A., "Development of a Runge–Kutta Scheme with Total Variation Diminishing for Magneto-gasdynamics," *Journal of Spacecraft and Rockets*, Vol. 39, No. 4, July–Aug. 2002, pp. 624–632.
doi:10.2514/2.3853

[20] Khan, O. U., Hoffmann, K. A., and Dietiker, J. F., "Computational Aspects of High Speed Flows with Applied Magnetic Field," *IEEE Transactions on Magnetics*, Vol. 42, No. 3, March 2006, pp. 389–397.
doi:10.1109/TMAG.2005.858289

[21] Khan, O. U., and Hoffmann, K. A., "Numerical Investigation of Decomposed Magnetofluid Dynamics Equations," *AIAA Journal*, Vol. 47, No. 11, Nov. 2009, pp. 2666–2675.
doi:10.2514/1.42626

G. Palmer
Associate Editor